Electrocatalytic Activity of Graphene Oxide/Metal Organic Framework Hybrid Composite on Hydrogen Evolution Reaction Properties

Mogwasha D. Makhafola[1], Kabelo E. Ramohlola[1], Thabiso C. Maponya[1], Thabang R. Somo[1], Emmanuel I. Iwuoha[2], Katlego Makgopa[3], Mpitloane J. Hato[1,4,], Kerileng M. Molapo[2], Kwena D. Modibane[1,*]*

[1] Nanotechnology Research Lab, Department of Chemistry, School of Physical and Mineral Sciences, University of Limpopo (Turfloop), Sovenga 0727, Polokwane, South Africa
[2] SensorLab, Chemistry Department, University of the Western Cape, Cape Town, South Africa
[3] Department of Chemistry, Faculty of Science, Tshwane University of Technology (Acardia Campus), Pretoria 0001, South Africa
[4] Department of Environmental Sciences, College of Agriculture and Environmental Sciences, University of South Africa, Florida Science Campus, Johannesburg 1710, South Africa
[*]E-mail: mpitloane.hato@ul.ac.za, kwena.modibane@ul.ac.za

In this work, the electrocatalytic activity of graphene oxide (GO) and its composite with metal organic framework (MOF) towards electrochemical hydrogen evolution reaction (HER) was studied. GO/MOF composite was synthesized by impregnation route and characterized using X-ray diffraction (XRD), Fourier transform infrared spectroscopy (FTIR), simultaneous thermal analysis (STA), scanning electron microscopy/energy dispersive spectroscopy (SEM/EDS) and high-resolution transmission electron microscopy/energy dispersive X-ray spectroscopy (HR-TEM/EDX). STA analysis showed an enhancement of the thermal stability of the GO/MOF composite compared to the pristine GO and MOF. SEM/EDS and HR-TEM/EDX confirmed the presence of octahedral structure of MOF in the GO sheet-like structure and elemental composition of the synthesized compounds. The performance of the proposed electrolytic system for electrochemical HER by Tafel parameters and turn over frequencies (TOFs) showed a huge increment of H_2 production in the composite through the Volmer reaction together with either of the two mechanisms in HER. This indicated that the addition of GO/MOF in the electrolytic system possessed better catalytic characteristics with enhanced TOFs, which may open a new way for hydrogen technology via HER enhancement.

1. INTRODUCTION

Global energy supply depends on fossil fuel combustion, which is the major contributor of environmental problems such as global warming and greenhouse emission. In order to avoid relying on fossil fuels as energy sources, hydrogen gas (H_2) as a renewable energy has been identified as the best energy source. The gas offers ideal characteristics which include lightweight, recyclability, fuel efficiency and environmental friendliness as compared to fossil fuel based sources [1-4]. In addition, H_2 gas gives high energy density of around 2.75 times in comparison with conventional gasoline based fuels [4]. In this regard, there is a need to produce H_2 with high purity for industrial applications [4, 5]. H_2 can be produced from various methods such as photo-induced natural gas reforming, coal gasification (syngas) as well as the electrolytic splitting of water [6, 7]. Among these methods, the splitting of water is ideal owing to its easiness and cost-effectiveness [7]. Water splitting consists of two half-cell reactions, viz; oxygen evolution (OER) and hydrogen evolution (HER) reactions [5-9] which occur on the anode and the cathode, respectively. Nowadays, platinum (Pt)-based catalysts or Pt are best choices to give best HER electrocatalytic performance in acid medium, boasting zero potential and diverse pH tolerance [7-10]. However, due to high cost and rare abundance of the platinum group metal (PGM) catalysts, preclude their large-scale applications. Hence, there is a great push in finding a cheaper and high earth abundant materials as alternatives to PGM for hydrogen evolution [5, 8, 9].

Transition metal-based compounds (TMCs) like oxides, selenides, sulfides, phosphides, carbides and nitrides have been regarded as alternatives to noble metal-free electrocatalysts. This is attributable to their high catalytic efficiency, potential and thermodynamic stability, diversity and abundant reserves [11-13]. Despite their HER performances, the TMCs show poor intrinsic properties and possess limited active sites which hamper their performances [14]. Carbonaceous materials, which include activated carbons, carbon nanotubes and graphenated compounds are electrochemically inert in nature. Thus they have been rarely used in electrochemical reactions, particularly HER [15]. Among these materials, graphenated materials such as graphene oxides (GO) have been extensively used as electroactive material supports in electrochemical applications. Their superiority is due to physicochemical properties such as large surface area, excellent conductivity, high flexibility for post-modification, mechanical strength and good stability [16, 17]. Theerthagiri and coworkers [18] reported on iron diselenides ($FeSe_2$) nanorods grown on graphene nanosheets surface. Electrochemical results showed that 30% $FeSe_2$/GO have high electrocatalytic activity with exchange cathodic current density of 9.68 mAcm^{-2} at overpotential (η) = 250 mV and Tafel slope (*b*), of 64 mVdec^{-1}. The enhanced electrocatalytic performance of this composite was attributable to electronic and chemical pairing between the reacting species. In contrast, GO offers a large surface area, which is essential for well distribution of $FeSe_2$ nanorods. This brings positive synergistic effect by coupling of both GO nanosheets and $FeSe_2$ nanorods. In another study, Mahale and Ingle [19] prepared nano-nickel decorated graphene (Ni-graphene) composite and evaluated their HER performance. They obtained improved HER performance with the current density of 10 mAcm^{-2} at η = 65 mV and the *b* value of 54 mVdec^{-1}. The improved performance was associated with the presence of GO, which possesses a strong affinity for hydrogen proton and stabilizes the adsorbed hydrogen proton. Furthermore, the Ni on the graphene surface increases electron density which brings the synergy and results in improved HER performance. On the other hand, metal

organic frameworks (MOFs) have occurred as hopeful class of versatile porous compounds for a widespread variety of applications because of large surface area (~800 $m^2.g^{-1}$), high porosity as well as tunable functionalities [9, 11]. MOFs are highly crystalline species consisting of metal ions joined together by organic ligands leading to the formation of framework structures [20, 21]. The synergism between GO and MOFs was reported by Petit and coworkers [22, 23]. The authors have shown that GO and MOF can interact through metallic centres of MOF and oxygen-containing groups of GO. This has resulted in enhancement in gas adsorptions. Herein, we present the electrocatalytic performance of GO/MOF hybrid composite as a new class of synergic electrocatalyst for HER applications. The Cu-based MOF (HKUST-1) was prepared by hydrothermal route, which can provide high crystallinity, possibility to control its morphology, controlled size as well as distribution of shape [8]. The GO/MOF composite was synthesized via a simple impregnation method and studied for electrochemical HER properties in acidic medium.

2. EXPERIMENTAL SECTION

2.1. Materials and reagents

Trimesic acid (H_3BTC), graphite powder, tetrabutylammonium percholate (TBAP), copper nitrate trihydrate ($Cu(NO_3)_2.3H_2O$), and sodium nitrate ($NaNO_3$) were purchased from Sigma Aldrich, South Africa. Sulphuric acid (H_2SO_4) dimethylformamide (DMF), dimethylsulfoxide (DMSO), and phosphoric acid (H_3PO_4) were procured from Rochelle Chemicals, South Africa. Potassium permanganate ($KMnO_4$) and hydrochloric acid (HCl) were purchased from SAARCHEM. Hydrogen peroxide (H_2O_2) was obtained from Moncon. The standard solutions of H_2SO_4 were prepared in TBAP/ DMSO (1:141 mole ratio) mixture as a supporting electrolyte at a temperature around 22±2 °C.

2.2. Synthesis of GO, MOF and GO/MOF composite

GO was prepared using a modified Hummers approach [24]. Briefly, graphite (5.0 g), 108 mL H_2SO_4, 12 mL H_3PO_4 and 2.5 g of $NaNO_3$ were mixed together under stirring in an ice bath for 10 minutes. This was followed by subsequent addition of $KMnO_4$ (15.0 g) into the mixture while keeping the temperature below 5 °C The resultant mixture was allowed to react for 2 hours. The temperature was increased to 98 °C for 60 minutes while water was added dropwise, and thereafter 15 mL of H_2O_2 was introduced into the solution. Deionized water and HCl were used to wash the product. Finally, the product was dried at 60 °C.

The synthesis of Cu-based MOF was done via the hydrothermal method as reported in our previous works [8, 9, 11, 25, 26]. An impregnation method, which is a direct mixing procedure, was used to prepare GO/MOF composite as given in Scheme 1. Briefly, a solution of MOF (0.1 g of MOF was added to 10 mL of DMF) and a solution of GO (0.1 g of graphene oxide (50 wt.%) in 1.4 mL of DMF) were mixed together and stirred magnetically for 24 hours at 50 °C. The prepared composite was filtered, washed with ethanol and dried at 50 °C for overnight.
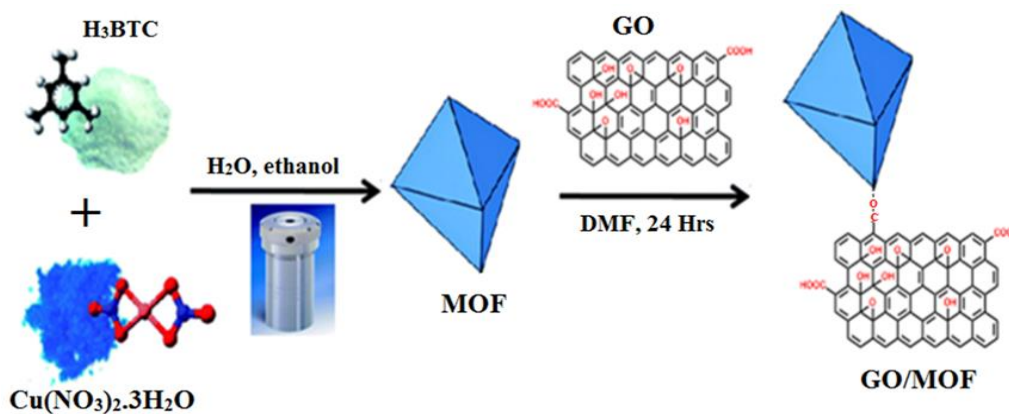
Scheme 1. Hydrothermal synthesis of MOF and a modest impregnation method for GO/MOF composite.

2.3. Physical Characterizations

FTIR spectra were obtained from a Spectrum II spectrometer (Perkin-Elmer) on a diamond ATR (400-4500 cm^{-1} at a resolution of 4 cm^{-1}). The X-ray diffraction (XRD) analysis was done using a system XRD Phillip PW 1830 diffractometer (CuK$_\alpha$ radiation, $\lambda = 1.5406$ Å). Thermal properties were obtained from a simultaneous thermal analyzer (STA Perkin-Elmer 4000) operated at 30-500 °C at a rate of 20 °C.min^{-1} under an inert atmosphere. High-resolution transmission electron microscopy (HR-TEM) and scanning electron microscopy (SEM) observations were acquired from HR-TEM, FEI Tecnai G2 F20X-Twin MAT 200-kV, Eindhoven, Netherlands and SEM, Auriga Field-emission SEM. Both systems were coupled with electron diffraction system for elemental analysis.

2.4. Electrochemical Characterizations

HER was performed in a three-electrode glass cell operating on an EPSILON electrochemical workstation. The Pt and gold electrodes with a diameter of 3 mm and an area of 0.071 cm^2 serve as auxiliary and working electrodes, whereas Ag/AgCl is the reference. Electrochemical measurements were conducted at 22±2 °C, potential window ranging between -1.0 to 1.0 V and scan rate of 0.02 - 0.10 V s^{-1} for multiscans of solutions of the synthesized materials (2.0 × 10^{-4} molL^{-1}) in 10 mL of TBAP/DMSO electrolyte (1:141 mole ratio). HER studies were carried out by varying the concentration of H$_2$SO$_4$ as H$_2$ source and ~2.0 x 10^{-4} molL^{-1} of GO and GO/MOF composite as catalysts.

3. RESULTS AND DISCUSSION

3.1. Structural Properties

The crystalline phases of the synthesized GO and GO/MOF composite were investigated using XRD (Fig. 1). In Fig. 1(a), the GO spectrum shows a strong diffraction peak at $2\theta \approx 10.5°$, corresponding to (002) plane of GO [25, 26]. By using the Bragg's equation, the estimated *d*-spacing was found to be 8.12 Å [5]. In the case of the composite (GO/MOF), well-defined sharp, intense peaks are noticeable, which indicate a highly crystalline structure of the composite [8, 9, 11, 26]. This behaviour suggests that

the structural phases and crystallinity of MOF were maintained upon composite formation. Notably, the intensity of the diffraction relating to (002) plane of GO decreased in the composite, suggesting that there is a possible electrostatic interaction between the GO and MOF (see Scheme 1).

The functional groups present in GO and composite were determined using FTIR (Fig. 1(b)). The FTIR spectrum of GO displays bands around 1060, 1450 and 1735 cm^{-1}, which are attributable to C-O, C-OH and C=O vibrations, respectively [22, 23, 27-33]. The vibration around 800 and 810 cm^{-1} can be assigned to epoxy/peroxide groups and C=O stretching vibration from sulfonic groups, respectively [22]. Moreover, GO/MOF ought to have appearance or disappearance of absorption bands, which is indicative of interactions between its pristine components (GO and MOF). The bands of both GO and MOF are clearly observed in the FTIR spectrum of the composite GO/MOF. However, there is a development of a new band appearing at 617 cm^{-1}, which is associated with the Cu-O stretching vibration [22, 23]. This is due to the oxygen of graphene oxide and copper metal centres on MOF. This result confirms that there is a plausible electrostatic interaction between the two parent materials as envisaged by the XRD results.
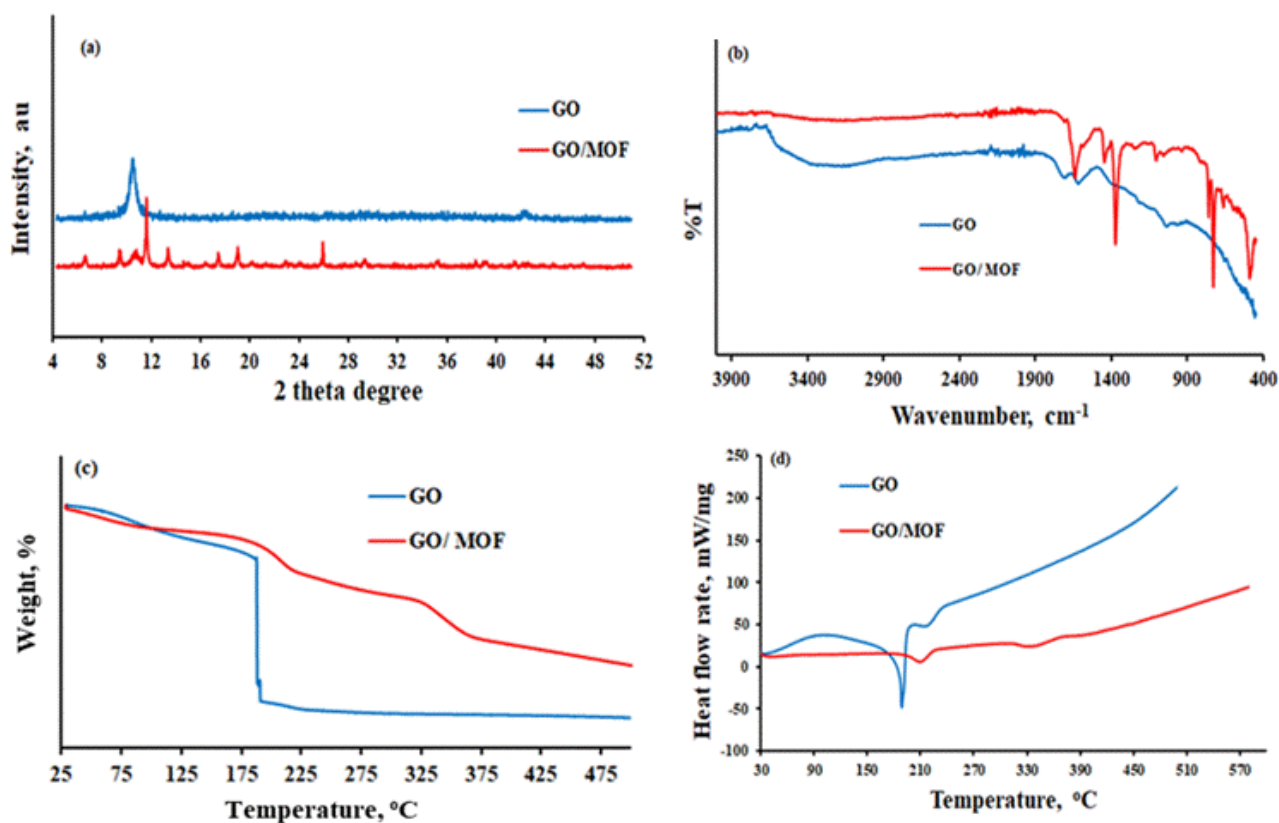

Figure 1. (a) XRD patterns, (b) FTIR spectra, (c) TGA and (d) DSC thermograms of GO and GO/MOF composite.

The STA analysis of the synthesized materials was exploited in the temperature range of 30–500 °C. consequence results are displayed in Fig. 1(c) and (d) for TGA and DSC, respectively. The TGA thermogram of GO shows two degradation steps at around 100 and 180 °C. The first degradation step is due to the loss of moisture and other solvents at low temperatures of less than 100 °C [34, 35]. The second step at 180 °C (60 wt. % mass loss) correspond to the decomposition of oxygen containing groups

of GO [34, 35]. As seen in Fig. 1(c), the GO/MOF composite exhibits enhancement in thermal and moisture stability as compared to bare GO, with the weight loss of about 19.0 wt%. The composite depicts three degradation steps at 75, 225 and 350 °C, corresponding to ethanol/moisture, GO and BTC decomposition in the structure of MOF, respectively. Furthermore, the composite shows lower mass loss with increasing the temperature, attributed to the internal change and strong interaction between GO and MOF. The DSC curve, shown in Fig. 1(d) by blue line, shows an endothermic peak at around 180 °C. This peak is due to absorption of heat as GO decomposes [36]. The DSC of the composite reveals that both GO and MOF are present, showing two exothermic peaks corresponding to decomposition temperatures of both GO and MOF. Additionally, the final degradation step took place at about 350 °C for GO and GO/MOF composite, with the later sample depicting a sudden weight loss in comparison to the former. This behaviour in which the composite shows slower and less steep degradation process possibly suggests an enhanced thermal stability [5, 8].

3.2. Morphological characterizations

The structures and morphologies of prepared materials were investigated using SEM (Fig. 2). The SEM image of GO given in Fig. 2(a) depicts some dense flakes of graphene sheets [36]. The imaging of the composite is quite different from the parent materials as expected. Fractures and corner breakage of the crystals, which occurred during admixing of the parent materials can be observed on the image of the composite [37, 38]. Upon composite formation, there is a clear obstruction of the development of MOF crystallites causing the reduction of crystallites of the composite as seen in Fig. 2(a) and the inset image. These observations coincide very well with the XRD results discussed. Petit and coworkers [22, 23] proposed that the composite formation is through the interaction between the Cu metal of MOF and the oxygen-comprising functional groups on GO. In addition, the magnification of the octahedral crystals of GO/MOF composite as depicted in Fig. 2(c) (inset) showed that the integration of GO into the composite resulted in coarse and rough morphological characteristics on the surface of MOF suggesting a possible interaction between MOF and GO through oxygen groups on GO and Cu of MOF [22]. The EDS spectra (Fig. 2(b) and (d)) show the elements present in GO and composite. The GO comprises of carbon and oxygen. These elements are clearly observed in Fig. 2(b). Since the elements in GO are also present in MOF, the composite GO/MOF shows enhancement in the composition of carbon (Fig. 2(d)). The EDS results validate the presence of small peaks of manganese, potassium, chlorine and phosphorus, which may be ascribed to impurities emanating from precursors during the synthesis process of GO and GO/MOF composite.
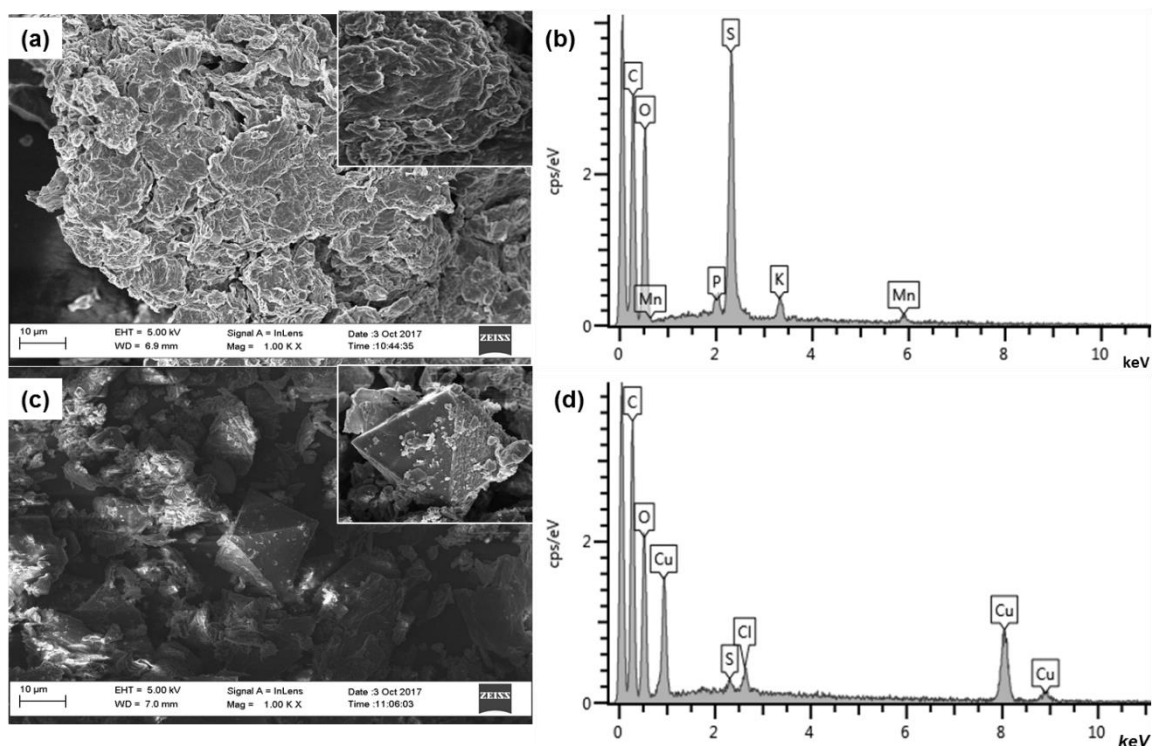
Figure 2. Morphological ((a) and (c)) and elemental ((b) and (d)) characterizations synthesized materials. (a) SEM micrograph of GO and (c) GO/MOF composite (inset: enlargement on the crystal structure to sight the surface of the crystal); (b) and (d) EDS spectra of GO and GO/MOF composite, respectively.

TEM photographs of GO and composite are presented in Fig. 3(a) and c), respectively. As seen in Fig. 3(a), the GO shows a well exfoliated graphene nanosheets and wrinkled transparent sheet-like structure. For GO/MOF composite given in Fig. 3(c), the layers are due to the interaction between MOF blocks and GO sheets. It was seen that the interaction is between the GO oxygen-containing functional groups and the MOF copper dimmers, resulting in chemical interactions upon formation of composites [23]. It is interesting to observe that upon the composite formation, the octahedral shape of MOF crystals [8] was maintained, demonstrating the constrain effects of layers of GO subsequent in preservation of the original shapes of the MOF crystals in their carbonized phase [23]. There is a clear separation between the graphene phase and the MOF phase, thus large aggregates can be distinguished easily. Moreover, the thin layers of graphene seem to have covered some of the MOF sites. The MOF can easily be broken down using electron beam illumination preventing any visualisation of its lattice structure [22]. Nonetheless, the pattern detected can be ascribed to the lattice micrographs of MOF in the composite. The crystalline structure of MOF was retained upon the incorporation of GO. This may be credited to the distorted layers of graphene, which dispersed the electrostatic charges [22, 23]. As shown in Fig. 3(b and d), the EDX spectra revealed all the elements present in MOF [8] GO, and GO/MOF composite. This results confirm a successful incorporation of GO onto MOF. In addition, there is an observable presence of K and S impurities. Fig. 4(a) and (c) present the HR-TEM images of GO and composite and SAED patterns (Fig. 4(b) and (d)).
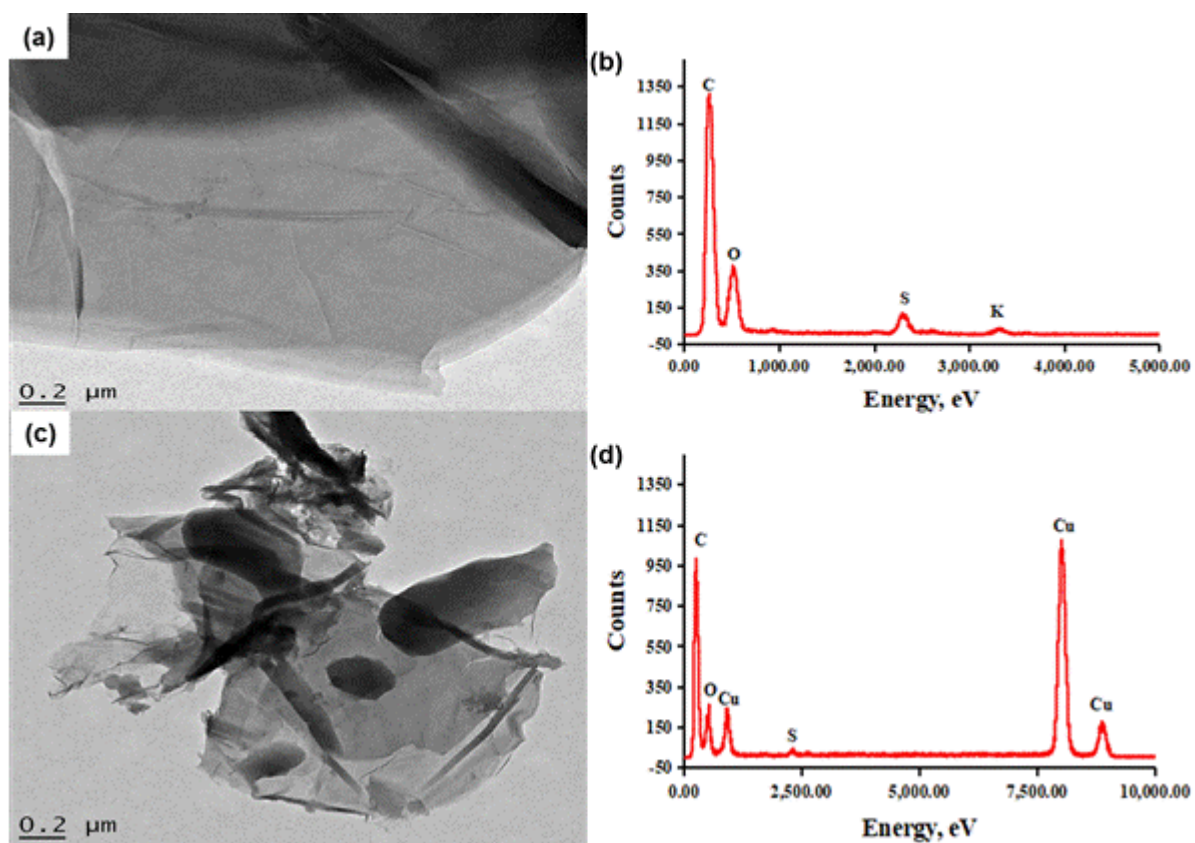
Figure 3. TEM images of (a) GO and (c) composite, EDX spectra (b) GO and (d) composite.
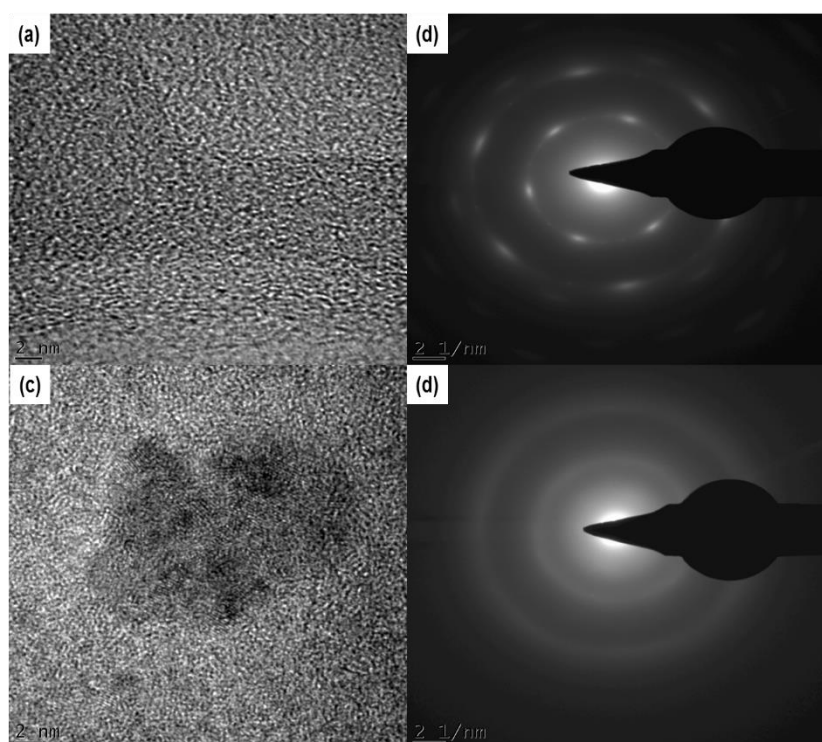

Figure 4. HR-TEM images of (a) GO and (c) composite; and SAED patterns of (b) GO and (d) composite.

It can be seen that both images of GO and GO/MOF composite clearly exhibit the existence of fringe lattices. The GO shows an amorphous characteristic of graphene sheet with a *d*-spacing of 1.08 nm [39]. The amorphous character of GO is supported by the SAED result showing absence of clear rings. Nonetheless, the GO/MOF images in Fig. 4(c) and (d) for HR-TEM and SAED images show that the *d*-spacing is 1.05 nm which is close to (222) and (002) planes of MOF and GO, respectively. Furthermore, the SAED pattern of the composite depicts well-defined rings, suggesting that the crystalline character of the GO has been improved. The HR-TEM results clearly suggest the successful formation of hybrid-structured GO/MOF and these observations are in good agreement with both XRD and SEM results.

3.3. Electrochemical characterization

Electrochemical behaviour of any material is very important in order to understand its redox characteristics. Figure 5 presents the electrochemical characteristics of GO and GO/MOF composite studied by cyclic voltammetry (CV) in TBAP/DMSO electrolyte (1:141 mole ratio). The graphene oxides (GO) exhibits characteristic cathodic reduction peaks at region of -0.500 and -0.750 V (vs. Ag/AgCl) owing to the reduction of epoxy, peroxy and aldehyde functional groups [22]. It was seen from the CV of GO that oxidation peak appeared at positive potential of 0.750 V coupled with one of the reduction peaks. It was stated that GO synthesized following permanganate oxidation methods, possessed two pairs of electrochemically reversible peaks as compared to one electrochemically irreversible inherent reduction peak of GO prepared from chlorate oxidation routes [34]. These reduction peaks of GO disappeared in GO/MOF material, suggesting that the formation of the composite was through interaction of the oxygen containing species with metal of MOF material. As clearly seen in the CV of GO/MOF on the gold electrode, it shows the diffusion of the redox mediator (Cu^{2+}/Cu^{+}) through their layers to the electrode surface [25,26,33]. Interestingly, the CV of the composite depicted the appearance of anodic peak towards potential of 0.250 V for conversion of Cu to Cu^{+} [33].
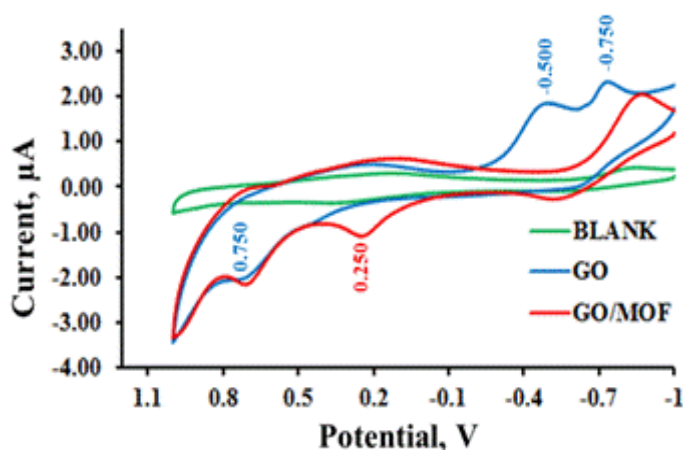

Figure 5. Cyclic voltammograms of Blank (Au electrode), GO and composite at scan rate of 0.1 Vs^{-1} in TBAP/DMSO electrolyte (1:141 mole ratio).

Fig. 6 (a) and (b) show multiscan voltammograms of GO and GO/MOF composite, respectively. As shown in Fig. 6(b), the peak currents corresponding to three copper processes a slow increase with the scan rate, whereas, the peak currents corresponding to the reverse processes increase with an increase in the scan rate and reach constant values. In addition, the Cu (III) formed and are used as catalysts to the HER process [32, 35]. Both the cathodic peak (I_{pc}) and anodic (I_{pa}) currents increase when the scan rate is increased from 0.1 to 1 Vs^{-1}. The electrochemical quasi-reversible process was observed in all the redox couples with respect to the cathodic peak current and anodic peak current (Ipc/Ipa) ratio and change in peak potential (ΔEp) values. In all scan rates (Fig. 6(c-d)), the unity of I_{pc}/I_{pa} ratios and the slope of 0.5 from plot of logarithm of the reductive peak current as a function of the logarithm of the scan rate reveals that all synthesized materials undergo diffusion controlled electrochemical redox processes [36, 37]. Furthermore, the diffusion coefficient, D, for catalysts was calculated using Randles-Sevcik equation for a quasi-reversible system (Equation 1) [36, 37].

$$Ip = (2.65 \times 10^5)n^{3/2}ACD^{1/2}(v)^{1/2} \tag{1}$$

Consistent with Equation 1, Fig. 5(c) showed that a linear increase in current was observed as the function of square root of the scan rate, $v^{1/2}$. The obtained D values were found to be 4.15 x 10^{-7} and 3.32 x 10^{-7} cm^{2}s^{-1} for GO and composite, respectively as an indication of first electron transfer [8, 36]. A similar trend was observed in MOF based polymer composite [29, 38].
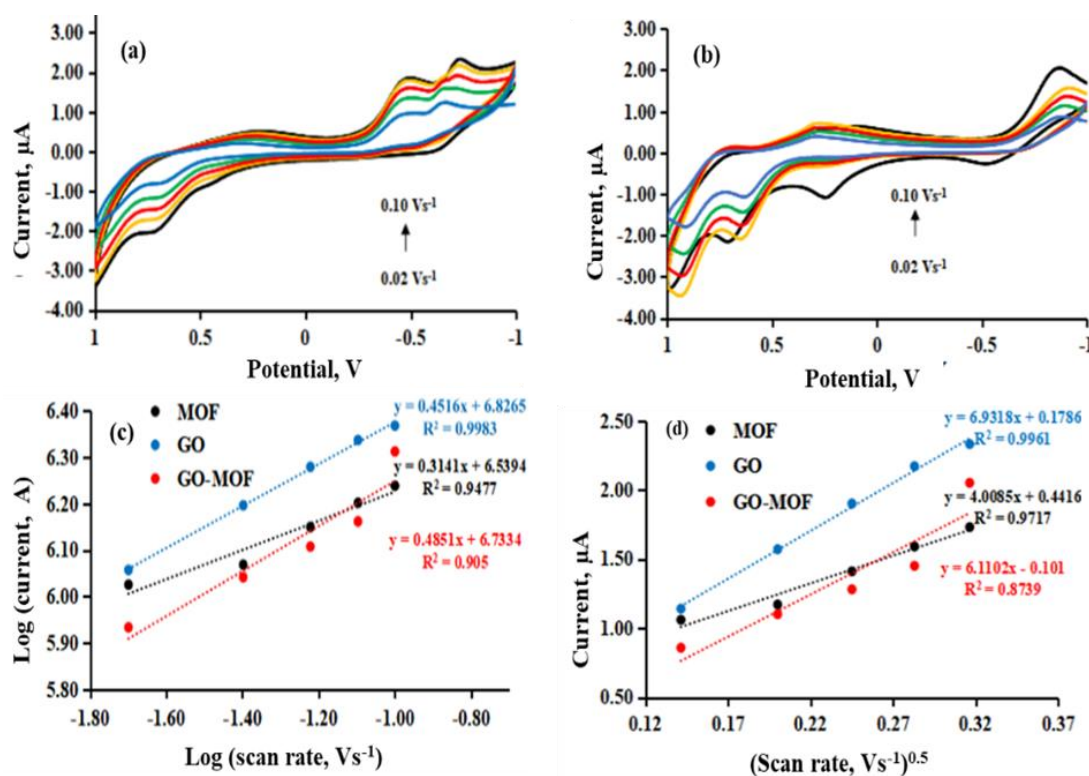

Figure 6. Cyclic voltammogram of (a) GO and (b) GO/MOF composite at different scan rates (0.02-0.1 v.s^{-1}); (c) The log-log plot of the absolute value of the peak current vs scan rate and (d) peak current as a function of square root of scan rate GO and GO/MOF as compared to MOF on Au electrode in TBAP/DMSO electrolyte (1:141 mole ratio).

3.4. Electrocatalytic Hydrogen Evolution studies

The CV was used to evaluate the HER studies of the samples in TBAP/DMSO electrolytic system (1:141 mole ratio) with H_2SO_4 as hydrogen source. Fig. 7(a) and (b) show the HER results GO and GO/MOF. A catalytic wave was observed near the reduction potential upon the introduction of H_2SO_4. This is evidence that H_2SO_4 is reduced to H_2 over GO and GO/MOF composite [29]. The amount of H_2 produced is depicted by the current intensities of the materials [25,29]. Therefore, high current readings imply large amount of H_2 produced. This observation is an indication that our samples possessed good electrocatalytic performance for HER [38]. Furthermore, the current intensity at -0.700 V corresponding to GO/MOF composite is large compared to that of GO.
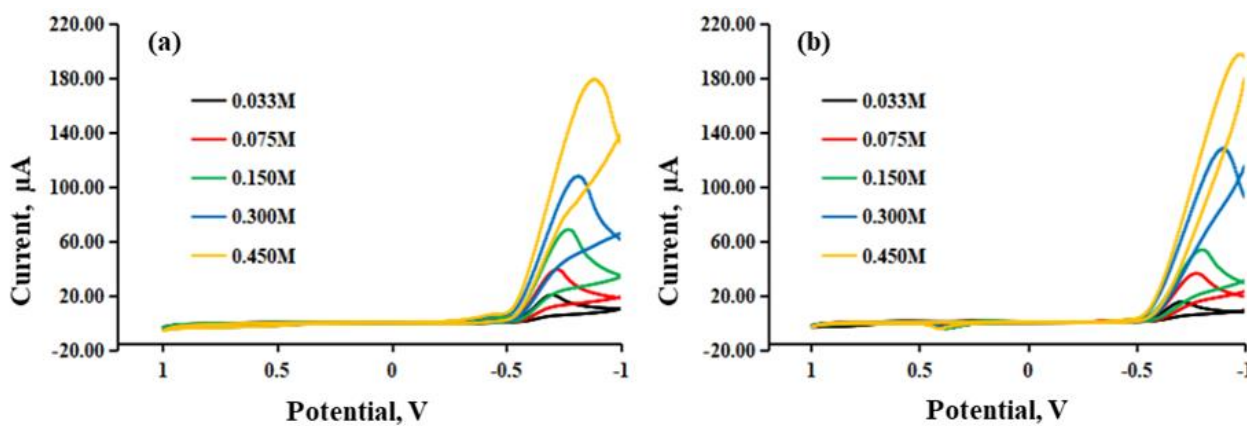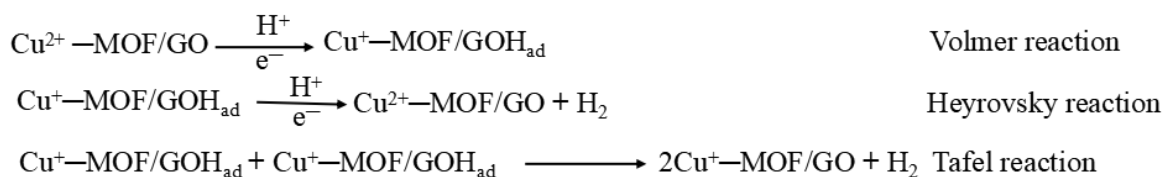

Figure 7. CV curves of (a) GO and (d) composite in various concentration of hydrogen source (0.033-0.450 $molL^{-1}$ H_2SO_4) at scan rate 0.10 Vs^{-1}.

The Tafel analysis provides information about the kinetics and activity of HER [39]. During electrochemical reaction, Tafel slope can be utilized to deduce the slowest step, which is the rate determining step. Additionally, the overall electrocatalytic HER mechanism in this work can also be proposed, as presented in Scheme 2. In an acidic medium, a HER reaction can take place via three steps. Initial reduction of Cu(II) to Cu(I) of the GO/MOF (represented by MOF/GO in Scheme 2 for better illustration). This is followed by interaction of the proton with the corresponding composite and leading in to formation of the composite hydride (MOF/GOH$_{ad}$) in hydrogen storage process. This as the most probable intermediate and proposed to be Volmer mechanism [25,26,33]. After the composite hydride, the hydride intermediate easily undergoes a protonation, or interacts with one another to form an H_2 molecule through a Heyrovsky or Tafel reaction.

$$Cu^{2+}-MOF/GO \xrightarrow[e^-]{H^+} Cu^+-MOF/GOH_{ad} \qquad\qquad \text{Volmer reaction}$$

$$Cu^+-MOF/GOH_{ad} \xrightarrow[e^-]{H^+} Cu^{2+}-MOF/GO + H_2 \qquad\qquad \text{Heyrovsky reaction}$$

$$Cu^+-MOF/GOH_{ad} + Cu^+-MOF/GOH_{ad} \longrightarrow 2Cu^+-MOF/GO + H_2 \quad \text{Tafel reaction}$$

Scheme 2. Proposed mechanisms involved in the HER kinetics of the synthesized GO/MOF composite

The Tafel plot was constructed from current density-potential data at various concentrations ranging from 0.033 to 0.450 molL^{-1} H$_2$SO$_4$. In heterogeneous hydrogen evolution reaction, the quasi-steady or steady state current, i, is measured over a certain overpotential range, η. A Tafel line, which is a linear plot of the log(i) against η, is then constructed. The exchange current density, i_0, which is the x-intercept of the plot, was also determined. The slope obtained from a Tafel line is not affected by the surface area of the material [37]. Ramohlola and coworkers [8,26,29,33], reported that in a multi-step proton transfer process, b could also serve as an indicator of one of the HER steps (Volmer, Heyrovsky and Tafel) and i_0 the measure of performance of an electrocatalyst. In this study, b and i_0 values were obtained by linear polarization curves [29,33]. The results are presented in Table 1. In addition, another important parameter that can provide insight of HER mechanism is the cathodic transfer coefficient (1-α). The high overpotential region was used to estimate the cathodic transfer coefficient where the simplified form of the Tafel (Butler-Volmer) equation (Equation 3) was used.

$$b = \frac{-2.303RT}{(1-\alpha)F} \tag{3}$$

Fig. 8 and Table 1 show Tafel plots and parameters, for blank electrode, GO and GO/MOF composite. In this study, it was observed that the GO has a Tafel slope of 144 mVdec^{-1} at 0.300 molL^{-1} H$_2$SO$_4$. At the same acid conditions, MOF and GO/MOF composite showed Tafel slope values which are low as compared to the pristine GO. The Volmer rate determining step during HER is observed when the Tafel slopes are between 105 to 150 mVdec^{-1} [40]. Nonetheless, the Tafel slope value was increased to 125 mVdec^{-1} upon the incorporation of GO and MOF. These findings agree with the work by Kubisztal and coworkers [41] when studying the HER behaviour of composites based on Ni coatings. In addition, the charge-transfer coefficient (α) was found to be close to $\alpha = 0.5$, which is indicative that the Volmer step is the rate-determining step. However, high slope values than 120 mV.dec^{-1} suggest that molecular hydrogen progression occurs with Volmer coupled with either Heyrovsky or Tafel step [43]. Table 1 shows that MOF and GO/MOF composite exhibited charge transfer coefficients that are not far from 0.5, indicating that the rate determining steps for these samples maybe the Volmer mechanism or Volmer mechanism coupled with one of the possibilities described above [40,41]. Furthermore, the turnover frequency (TOF) can be used to evaluate the efficiency of catalysts, as well as to assess electrocatalytic reactions. The TOF can be determined using Equation 4 [42]:

$$TOF = \frac{jM}{2Fm} \tag{4}$$

where j represents current density, M is the mass percentage of prepared materials, F defines the Faraday's constant, while m denotes the mass per square centimetre of MOF, GO and GO/MOF catalysts estimated from BET surface area of MOF (614. 7 m^{2}g^{-1} [25]) and GO (423 m^{2}g^{-1} [43]). The TOF values for GO and GO/MOF are presented in the Table 1. It was seen that the composite resulted in the enhancement of the TOF values. For example, the value was obtained to be 6.6 mol H$_2$s^{-1} as compared to 4.75 mol H$_2$s^{-1} of GO at 0.45 molL^{-1}. Another important characteristic of the kinetic parameter is the reaction order of HER; which provides additional information about the fundamental mechanism. Figure

9 depicts the pH dependence of the j_0 and the potential for the experimental data in this study. The apparent reaction order is represented by the slope of the trendline in Figure 9(a) ($\log(i)$ vs. pH). The apparent reaction order was determined to be around 0.8, suggesting a mixed type mechanism [44] as observed in Tafel parameters. Furthermore, in Fig. 9(b), which is a representation of the Pourbaix diagram, the slope was seen to be less than 0.5. The observed dependence agrees well with the proposed mechanism of the process above.
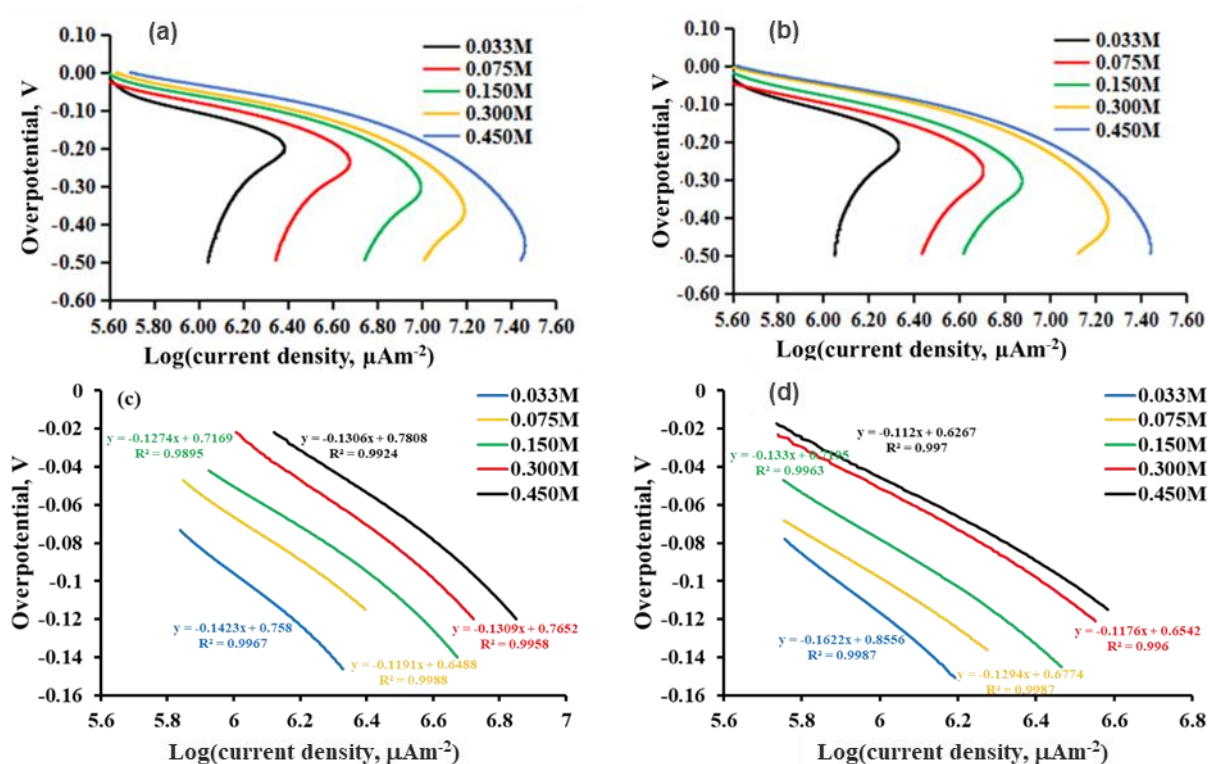

Figure 8. Polarization curves of overpotential as a function of concentration for (a) GO and (b) GO/MOF composite; and Tafel plots for (c) GO and (d) GO/MOF composite in different concentrations of H_2SO_4 at 0.10 Vs^{-1} scan rate on Au electrode in TBAP/DMSO electrolyte (1:141 mole ratio).
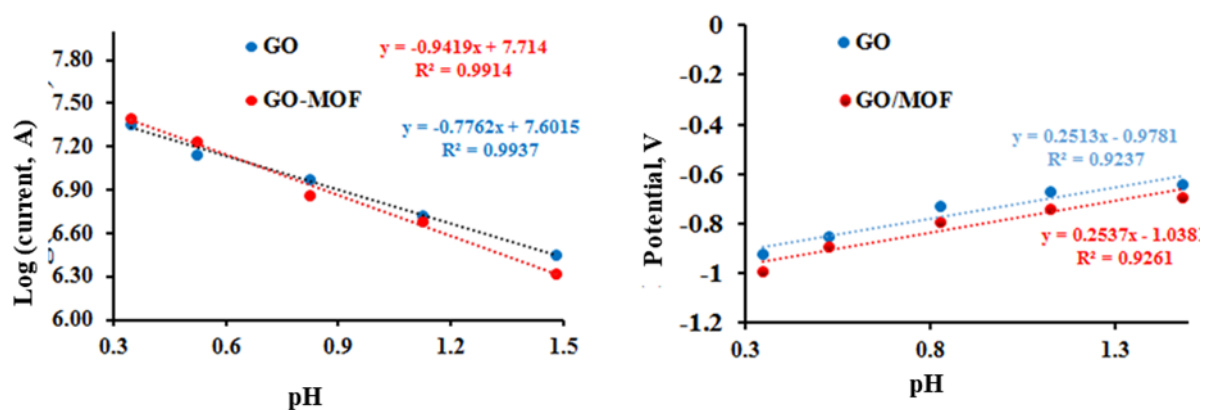

Figure 2. (a) Plot of log current as a function of pH of the solution and (b) Pourbaix diagram of HER.

Table 1. The (b), ($1-\alpha$), (j_0) and TOF parameters of GO and GO/MOF composite.

Material	H_2SO_4 (mol.L^{-1})	$-b$ (mV.dec^{-1})	$1-\alpha$	logi_0 (μA.m^{-2})	i_0 (A.m^{-2})	TOF (mol.H$_2$s^{-1})
GO	0.033	139	0.43	6.45	2.82	0.584
	0.075	176	0.34	6.73	5.37	1.113
	0.150	138	0.43	6.98	9.55	1.979
	0.300	144	0.41	7.15	14.13	2.928
	0.450	189	0.31	7.36	22.91	4.748
GO/MOF	0.033	157	0.38	6.32	2.09	0.550
	0.075	153	0.39	6.69	4.90	1.288
	0.150	142	0.42	6.87	7.41	1.950
	0.300	125	0.47	7.24	17.38	4.571
	0.450	116	0.51	7.40	25.12	6.607
Pd@CuPc/MOF [31]	0.300	177	0.33	7.00	8.9	
FeSe$_2$/GO [18]	0.500	64	-	-	-	-
Ni-graphene [19]	1.000[a]	54	-	-	-	-
TNCuPc/MOF [9]	0.300	191	0.31	5.95	0.889	-
WS$_2$/rGO [45]	0.500	58	-	-	-	-

a = KOH mol.L-1

4. CONCLUSIONS

In this work, GO/MOF composite for hydrogen production via the HER process was synthesized by the impregnation method of MOF and GO. The morphological and structural changes of MOF as a result of the GO incorporation were then assessed. Furthermore, the electro-catalytic activity of the samples in hydrogen evolution was subsequently studied. The enhancement of the HER exchange current density and reduction of the electrochemical reaction resistance were observed upon the introduction of GO. The observed improvement in HER studies upon the incorporation of GO is ascribed to the synergetic combination of GO and the MOF crystals, promoting an accelerated facilitation of HER as part of hydrogen production with enhanced TOF values. Furthermore, the Tafel slope and charge-transfer coefficients were used to determine the rate determining step supported by slopes from the plot of log current vs pH and Pourbaix diagram. The results demonstrated that microstructured GO based composite is suitable for hydrogen fuel cell applications.

References

1. K. Hareesh, S.D. Dhole, D.M. Phase, J.F. Williams, *Mater. Res. Bull.,* 110 (2019) 82.
2. Z. Wu, Z. Zou, J. Huang, F. Gao, *J. Catal.,* 358 (2018) 243.
3. M. Ahmed, I. Dincer, *Int. J. Hydrogen Energy,* 44 (2019) 2474.
4. I. Dincer, C. Acar, *Int. J. Hydrogen Energy,* 40 (2014) 11094.
5. G. Mashao, K.E. Ramohlola, S.B. Mdluli, G.R. Monama, M.J. Hato, K. Makgopa, K.M Molapo, M.E. Ramoroka, E.I. Iwuoha, K.D. Modibane, *Mater. Chem. Phys.*, 230 (2019) 287.
6. Á. Vass, Z. Pászti, S. Bálint, P Németh, A. Tompos, E. Tálas, *Mater. Res. Bull.*, 95 (2017) 71.
7. J. Xu, *Int. J. Electrochem. Sci.,* 12 (2017) 2253.
8. K.E. Ramohlola, G.R. Monana, M.J. Hato, K.D. Modibane, K.M. Molapo, M. Masikini, S.B. Mduli, E.I. Iwuoha, *Compos. Part B Eng.,* 137 (2018) 129.
9. G.R. Monama, M.J Hato, K.E. Ramohlola, T.C. Maponya, S.B. Mdluli, K.M. Molapo, K.D. Modibane, E.I. Iwuoha, K. Makgopa, M.D. Teffu, *Results Phys.*,15 (2019) 102564.
10. Y. Wang, Y. Zhao, A. Wu, Z. Dong, J. Li, J. Wang, *Int. J. Electrochem. Sci.,* 13 (2018) 10848.
11. G.R. Monama, S.B. Mdluli, G. Mashao, M.D. Makhafola, K.E. Ramohlola, K.M. Molapo, M.J. Hato, K. Makgopa, E.I. Iwuoha, K.D. Modibane, *Renew. Energy,* 119 (2018) 62.
12. Y. Zhang, Q. Shao, S. Long, X. Huang, *Nano Energy*, 45 (2018) 448.
13. C. Xuan, Z. Peng, K. Xia, J. Wang, W. Xiao, W. Lei, M. Gong, T. Huang, D. Wang, *Electrochim. Acta* 258 (2017) 423.
14. Y. Wen, H. Zhu, L. Zhang, S. Zhang, M. Zhang, M. Du, *Mater. Res. Bull.*, 112 (2019) 46.
15. L. Zhang, J. Xiao, H. Wang, M. Shao, *ACS Catal.,* 7 (2017) 7855.
16. J. Li, Z. Zhao,Y. Ma, Y. Qu, *Chem. Cat. Chem.*, 9 (2017) 1554.
17. Y. Liu, Z. Kang, *Mater. Res. Bull.,* 74 (2016) 441.
18. J. Theerthagiri, R. Sudha, K. Premnath, P. Arunachalam, J. Madhavan, A.M. Al-Mayouf, *Int. J. Hydrogen Energy,* 42 (2017) 13020.
19. N. Mahale, S.T. Ingle, *Energy,* 119 (2017) 872.
20. J. Lin, J. He, F. Qi, B. Zheng, X. Wang, B. Yu, K. Zhou, W. Zhang, Y. Li, Y. Chen, *Electrochim. Acta,* 247 (2017) 258.
21. Y. Li, R. T. Yang, *J. Am. Chem. Soc.*, 128 (2006) 726.
22. C. Petit, J. Burress, T. J. Bandosz, *Carbon,* 49 (2011) 563.
23. C. Petit, T. J. Bandosz, *J. Colloid Interface Sci.,* 447 (2015) 139.
24. J. Song, X. Wang, C.T. Chang, *J. Nanomater.,* (2014) 1.
25. G.R. Monama, K.D. Modibane, K.E. Ramohlola, K.M. Molapo, M.J. Hato, M.D. Makhafola, G. Mashao, S.B. Mdluli, E.I. Iwuoha, *Int. J. of Hydrogen Energy*, 44 (2019) 18891.
26. K.E. Ramohlola, M. Masikini, S.B. Mdluli, G.R. Monama, M.J. Hato, K. M. Molapo, E.I. Iwuoha, K. D. Modibane, *Electrochim. Acta,* 246 (2017) 1174.
27. B.D. Ryu, M. Han, K.B. Ko, K.H. Lee, T.V. Cuong, N. Han, K. Kim, J.H. Ryu, N.J. Park, Y. Lim, D.T. Thanh, C.H. Jo, K. Ju, C.H. Hong. *Mater. Res. Bull.,* 110 (2019) 76.
28. J. Liu, H. Jeong, J. Liu, K. Lee, J.Y. Park, Y. H. Ahn, S. Lee, *Carbon,* 48 (2010) 2282.
29. K.E. Ramohlola, G.R. Monana, M.J. Hato, K.D. Modibane, K.M. Molapo, M. Masikini, S.B. Mduli, E.I. Iwuoha, In: Kaneko S. et al. (eds) Carbon-related Materials in Recognition of Nobel Lectures by Prof. Akira Suzuki in ICCE. Springer, Cham.

30.   C. Petit, M. Seredych, T. J. Bandosz, *J. Mater. Chem. A,* 19 (2009) 9176.
31.   A. Olad, H. Bakht, K. Hagh, *Compos. B. Eng.*162 (2019) 692.
32.   Z. Li, O. Johnson, J. Huang, T. Feng, C. Yang, Z. Liu, W. Chen, *Mater. Res. Bull.*, 106 (2018) 365.
33.   K.E. Ramohlola, M. Masikini, S.B. Mdluli, G.R. Monama, M.J. Hato, K. M. Molapo, E.I. Iwuoha, K. D. Modibane *Int. J. Electrochem. Sci.,* 12 (2017) 4392.
34.   D.A. Brownson, G.C. Smith, C.E. Banks, *R. Soc. Open Sci.*, 4 (2017) 1.
35.   M. Devi, A. Kumar, *Mater. Res. Bull.*, 97 (2018) 207–214.
36.   J. Shen, Y. Hu, M. Shi, X. Lu, C. Qin, C. Li, M. Ye, *Chem. Mater.,* 21 (2009) 3514.
37.   Y. Zhao, Y. Cao, Q. Zhong, *J. Clean Energy Technol.*, 2(2014) 1–3.
38.   L. Li, X. L. Liu, H. Y. Geng, B. Hu, G. W. Song, and Z. S. Xu, *J. Mater. Chem. A*, 1 (2013) 10292.
39.   L. Zhang, C. Ye, X. Li, Y. Ding, H. Liang, G. Zhao, Y. Wang, *Nano-Micro Lett.,* 10 (2018) 28.
40.   B. Guo, H. Li, H. Song, Y. Zhang, X. Lei, H. Fu, Y. Ta, Z. Zhu, *ACS Appl. Mater. Interfaces*, 8 (2016) 5517.
41.   J. Kubisztal, A. Budniok, *Int. J. Hydrogen Energy*, 32 (2007) 1211.
42.   G. Mashao, K.D. Modibane, S.B. Mdluli, E.I. Iwuoha, M.J. Hato, K. Makgopa, K.M. Molapo, *Electrocatalysis*, 10 (2019) 406.
43.   Y. Gao, D. Ma, C. Wang, J. Guan, X. Bao, *Structure,* 47 (2011) 2432.
44.   L. Giordano, B. Han, M. Risch, W. T. Hong, R. R. Rao, K. A. Stoerzinger, Y. Shao-Horn, *Catal. Today*, 262 (2016) 2